

**Influence of a low-Z thin substrate on a microwire hard x-ray source driven by a picosecond laser pulse for point-projection x-ray radiography**

Meng-Ting, L.; Guang-Yue, H.; Huang, L.; Jian, Z.;

Originally published:

December 2020

**Physics of Plasmas 27(2020)123107**

DOI: <https://doi.org/10.1063/5.0023189>

Perma-Link to Publication Repository of HZDR:

<https://www.hzdr.de/publications/Publ-31997>

Release of the secondary publication  
on the basis of the German Copyright Law § 38 Section 4.

This is the author's peer reviewed, accepted manuscript. However, the online version of record will be different from this version once it has been copyedited and typeset.

PLEASE CITE THIS ARTICLE AS DOI: 10.1063/1.50023189

## Influence of a low-Z thin substrate on a microwire hard x-ray source driven by a picosecond laser pulse for point-projection x-ray radiography

Meng-ting Li<sup>1</sup>, Guang-yue Hu<sup>1,2</sup>, Lin-gen Huang<sup>\*,3</sup>, Jian Zheng<sup>1,4</sup>

<sup>1</sup>CAS Key Laboratory of Geospace Environment & Department of Engineering and Applied Physics, University of Science and Technology of China, Hefei, Anhui 230026, China

<sup>2</sup>CAS Center for Excellence in Ultra-intense Laser Science(CEULS), Shanghai 200031, China

<sup>3</sup>Helmholtz-Zentrum Dresden-Rossendorf (HZDR), Bautzner Landstraße 400, D-01328 Dresden, Germany

<sup>4</sup>Collaborative Innovation Center of IFSA (CICIFSA), Shanghai Jiao Tong University, Shanghai 200240, China

\*E-mail: gyhu@ustc.edu.cn

\*\* E-mail: lingen.huang@hzdr.de

In the point-projection hard x-ray radiography of dense matter, for example, an inertial confinement fusion implosion capsule at stagnation time, a picosecond laser driven gold microwire is used to produce a short pulse point, bremsstrahlung hard x-ray source. The microwire was held by a low-Z CH thin substrate commonly used to promote experimental performance. We explored the influence of the low-Z thin substrate on the microwire bremsstrahlung hard x-ray source via Particle-in-Cell (PIC) and Monte Carlo simulations. It was shown that both of the microwires, with or without the low-Z thin substrate, could emit more intense hard x-ray radiation than the radiator buried in equal-density substrate, which benefitted from efficient electron recirculation. The freestanding microwire exhibited further enhanced electron recirculation compared to that with the low-Z thin substrate, while the increased hot electrons were only present for the energetic electrons of  $>1$  MeV. Thus, the freestanding microwire could produce significantly more intense MeV gamma x-ray emission with respect to that with the substrate, but an ignorable increment was exhibited at the softer x-ray emission of 10–200 keV. These results provided valuable insights into the design of backlighter targets in point-projection x-ray radiography, such as a freestanding microwire being preferred in MeV gamma-ray radiography, while the microwire with the CH thin substrate could be used in the 10–200 keV hard x-ray Compton radiography of an implosion capsule.

### I. INTRODUCTION

This is the author's peer reviewed, accepted manuscript. However, the online version of record will be different from this version once it has been copyedited and typeset.

PLEASE CITE THIS ARTICLE AS DOI: 10.1063/1.50023189

A compressed implosion capsule at stagnation time determines the fusion gain directly in inertial confinement fusion (ICF) [1], which is sensitive to driven symmetry and hydrodynamic instabilities. The instantaneous and small size characteristics of a capsule at the stagnation phase ( $<150$  ps,  $\sim 150$   $\mu\text{m}$ ) require hard x-ray radiography with 10 ps temporal and 10  $\mu\text{m}$  spatial resolutions to diagnose a structure, which is difficult for traditional area backlighting x-ray radiography using a gated camera [2, 3]. Thus, point-projection hard x-ray radiography has been proposed to fulfill the demands in terms of temporal and spatial resolutions [4-7], for which a picosecond intense laser of  $<10$  ps duration irradiates a gold microwire with a 10- $\mu\text{m}$  diameter to generate a short pulse point hard x-ray source. This type of point-projection hard x-ray radiography can also be used in detecting shock waves [8, 9] or dense matter [10].

$K_{\alpha}$  line emissions have previously been adapted as the x-ray source to probe the dense matter [11-18], but the intensity of the  $K_{\alpha}$  source dropped rapidly in the harder x-ray range of  $> 20$  keV (typically  $\sim 10^{-5}$  to  $10^{-4}$  of the laser energy [19]). Above 70 keV, the bremsstrahlung continuous emissions had significantly more flux than  $K_{\alpha}$  line emissions [4]. Therefore, a 70-200 keV bremsstrahlung hard x-ray source was used in the Compton radiography of an ICF implosion [4-7]. This source could produce proper image contrast and depress the x-ray noise of capsule self-emission. The cross-section of the Compton scattering [20] and the spectral response of the detector (such as the Image Plate) [21] were insensitive to the x-ray photon energy from several tens of keV to hundreds of keV, which made the diagnosis more feasible in experiments.

Electron recirculation is an important phenomenon in ultra-short laser-target interaction, and it alters the dynamics of hot electrons [22-26] and x-ray emission [27-34]. The hot electrons that are accelerated by a relativistic laser pulse [35, 36] either transport into a target, knocking out bound electrons from inner shells and leading to line emissions, or collide with the atoms which produces bremsstrahlung continuous emissions. A fraction of the hot electrons escapes from the target and establishes sheath electric fields and quasi-static magnetic fields at the target surfaces. Most of the hot electrons are reflected by the quasi-static fields, travelling back and forth between the front and rear surfaces and being re-accelerated by the laser field until they escape or exhaust their energy in the target. Electron recirculation has an important contribution to both  $K_{\alpha}$  line emissions [27-32] and bremsstrahlung emissions [33, 34]. The  $K_{\alpha}$  line emissions can be increased by one order of magnitude, depending on the laser intensities. Additionally, the  $K_{\alpha}$  emission isotropy [37] and source size [38] can be altered. In our previous investigation of a planar foil target [39], we found that the bremsstrahlung hard x-ray emission could be enhanced by several orders of magnitude due to the electron recirculation.

In point-projection x-ray radiography, a 10- $\mu\text{m}$  diameter gold microwire (300- $\mu\text{m}$  length) [5] is aligned along a radiography axis. An end-view of gold wire presents a point x-ray source with an effective source size for the wire diameter. Unfortunately, gold wire is soft and it inclines easily, which will obviously increase an x-ray source size. Thus, typically a low-Z substrate of CH plastic foil with 10- $\mu\text{m}$  thickness is attached to it to ease target manufacture (5- $\mu\text{m}$  aluminum foil was used at first [40], but it was replaced by CH foil soon due to the stronger x-ray noise of aluminum foil [5]). The substrate can also ease the pointing of a short pulse beam to the gold wire or avoid transmission of the laser pulse through the wire. Our previous simulations and experiments showed that this substrate should be low-Z material such as CH to avoid x-ray noise [39]. However, the influence of 10- $\mu\text{m}$  CH plastic thin substrate on the hard x-ray source emitted from a gold microwire was unclear yet, which is investigated in this work. As could be expected, the thin substrate altered the electron recirculation or the laser absorption (the laser focus spot was larger than the diameter of the wire), which likely changed the hard x-ray emitted from the microwire.

In this research, we explored the influence of 10- $\mu\text{m}$  thickness low-Z substrate on the hard x-ray source radiated from a 10- $\mu\text{m}$  diameter gold microwire through Particle-in-Cell (PIC) and Monte Carlo simulations. We compared the hot electron generation and hard x-rays emitted from the gold microwires with four geometries: buried in the equal-density thick foil or thin foil, held by a low-Z substrate, and freestanding microwire without substance. It was found that both of the microwires, with or without a low-Z substrate, generated more intense hard x-ray emission than those buried in equal-

density foils mainly due to the electron recirculation. With respect to the microwires with a low-Z substrate, the freestanding microwire exhibited more intense MeV gamma x-ray emission. However, the hard x-ray for 10–200 keV had no obvious difference between them.

## II. SIMULATION MODELS

2D3V PIC and 3D Monte Carlo codes were used in our simulations, as described in our previous work [39]. Generally, the PIC simulations gave the energy spectra and angular distributions of laser generated hot electrons in the laser-target interaction. Then the PIC output was coupled into the Monte Carlo code to calculate the emission of x-rays.

### A. Setup of 2D3V PIC to simulate the generation of the hot electrons

Figure 1. Scheme of the 2D3V PIC simulations of the laser-target interaction. (a) Thick gold foil without electron recirculation. (b) Thin gold foil with 10- $\mu\text{m}$  thickness. (c) 10  $\mu\text{m} \times 10 \mu\text{m}$  gold wire with a CH substrate with a 10  $\mu\text{m}$  thickness. (d) Freestanding gold wire with dimensions of 10  $\mu\text{m} \times 10 \mu\text{m}$ . The rear surface of the thick gold foil was attached to the boundary of the simulation area at  $x = 90 \mu\text{m}$ . The main targets and the preplasmas are distinguished by white dashed lines in (a), (b) and (c). Their densities are represented by different colors, as described in the text. The curves above the pseudo-color images express the density change along the X-axis and along the red dashed line in (d). The white arrows indicate the direction of the incident lasers. The white solid line squares are the probe boxes with dimensions of 10  $\mu\text{m} \times 10 \mu\text{m}$  that were used to count the electron motion crossing the four boundaries of the gold wire.

The laser absorption and hot electrons generation were modeled using the PIC code PICLS [41] in the (X, Y) plane, as illustrated in figure 1. In our 2D PIC simulations, the intensity of the laser pulse was written as  $I(y, t) = I_0 e^{-4 \ln 2 [(y-y_0)/\phi_{\text{FWHM}}]^2} e^{-4 \ln 2 [(t-t_0)/\tau_{\text{FWHM}}]^2}$ , where  $I_0 = 4.4 \times 10^{18} \text{ W/cm}^2$  was the peak laser intensity,  $\phi_{\text{FWHM}} = 30 \mu\text{m}$  and  $\tau_{\text{FWHM}} = 0.6 \text{ ps}$  were the full width half maximum (FWHM) spot size and pulse duration respectively,  $y_0 = 0$  was the transverse center position of the target, and  $t_0 = 0$  was the reference time when the peak intensity irradiating on the front surface of the target. We assumed the laser energy in 3D geometry having a radial symmetric Gaussian intensity profile with the same spot size as 2D, written as  $I(r, t) = I_0 e^{-4 \ln 2 [(r-r_0)/\phi_{\text{FWHM}}]^2} e^{-4 \ln 2 [(t-t_0)/\tau_{\text{FWHM}}]^2}$ , then the conversion factor of the laser energy from 2D to 3D geometry was  $\alpha = \iint I(r, t) 2\pi r dr dt / \iint I(y, t) dy dt = \sqrt{\pi/4 \ln(2)} \phi_{\text{FWHM}}$ . Thus, the real particle numbers in the hot electron energy spectra were obtained by multiplying the linear densities by a transverse dimension (along the missing z axis), equal to  $\alpha$ . The laser pulse is p-polarization, and incidence at  $45^\circ$  with respect to the target normal. The cell size was  $\Delta x = \Delta y = 1/40 \mu\text{m}$  with five macroparticles per cell. The cell size was considered to resolved the plasma wavelength with reduced density in our simulations. The ions were immobile. The boundary conditions for the fields were periodic at the transverse boundaries ( $y = -90 \mu\text{m}, 90 \mu\text{m}$ ) and absorbent at the longitudinal boundaries ( $x = 0, 90 \mu\text{m}$ ), and for the particles, the boundary conditions were thermal reflecting in order to keep the total charge equal to zero. The total simulation time was 2 ps.

Four kinds of 10  $\mu\text{m} \times 10 \mu\text{m}$  gold wire geometries were investigated: (a) thick gold foil without electron recirculation, (b) thin gold foil with a 10- $\mu\text{m}$  thickness, (c) 10  $\mu\text{m} \times 10 \mu\text{m}$  gold wire with a 10- $\mu\text{m}$  low-Z substrate, and (d) 10  $\mu\text{m} \times 10 \mu\text{m}$  freestanding gold wire. The thick and thin gold foils in (a, b) were the reference cases for comparison, which were considered to mimic the gold microwires buried in equal-density substrates. To save the computational time, the density of the gold wire was reduced to  $5n_c$ , where  $n_c = 1.1 \times 10^{21} \text{ cm}^{-3}$  was the critical density. The low-Z CH substrate in (c) was modelled with  $2n_c$  density. The choice of the reduced density was followed by A. Compant La Fontaine et al.'s work [33]. In our simulations, the normalized peak laser electric field was  $a_0 = 0.85 \lambda [\mu\text{m}] \sqrt{I [10^{18} \text{ W/cm}^2]} = 1.88$ . Thus, the choice

of  $5n_c$  and  $2n_c$  for Au and CH was higher than the relativistic critical density  $\sim a_0 n_c$ , and therefore overdense for such laser intensity. So it was reasonable to use the reduced densities to simulate the hot electron generation in PIC since the laser field decays quickly near the relativistic critical density surface, although it was not realistic to simulate the hot electron transport and thus x-ray radiation which strongly depended on the target density and charge state distribution. To leverage between the computational power and quantitative comparison to the experiments, the hot electron transport was simulated by the Monte Carlo code Geant4, which used the realistic mass density of gold by coupling the input of hot electron spectra and angular distributions from PIC simulations.

The targets consisted of dense main plasmas and under-dense preplasmas. The electron density profile of the preplasmas in front of the gold and CH substrate were set to be  $n_e(x) = n_0 \exp(-(x - 60)/L_p)$ , where  $L_p = 6 \mu\text{m}$  is the preplasma scale length and  $x = 60 \mu\text{m}$  is the position of the main target's front surface.  $n_0$  is the density of main target, which was  $5n_c$  for the gold and  $2n_c$  for the low-Z CH substrate. The preplasmas had a one-dimensional exponential profile along the x-direction, shown in (a, b, c) and a radial exponential profile, shown in (d). The regions of  $0 < x < 4 \mu\text{m}$  and  $x > 70 \mu\text{m}$  were vacuum.

Only the  $10 \mu\text{m} \times 10 \mu\text{m}$  central square regions of the gold foils were chosen as the probe boxes to diagnose the outgoing hot electrons, which were consistent to the position of the  $10 \mu\text{m} \times 10 \mu\text{m}$  gold wire. When an electron with an energy of more than 50 keV escaping from the probe boxes, it was taken into account to calculate the energy and angular distributions. The energy and angular distributions of all the counted hot electrons from the PIC simulations were then coupled into the Monte Carlo code Geant4 to simulate the x-ray emissions.

### B. Setup of Monte Carlo Geant4 to simulate the x-ray emissions

Figure 2. Illustration of the Monte Carlo simulations using Geant4 code. The gold targets with dimensions of  $5 \text{ mm} \times 5 \text{ mm} \times 10 \mu\text{m}$  were shown (not scaled). The blue arrow indicated the direction of electron incidence. The red lines represented the electrons passing through the target and the green lines represented the emitted photons.

We used the Monte Carlo Geant4 code [42] to calculate the bremsstrahlung hard x-ray emissions of the gold microwire. The square gold wire was simplified as a  $10\text{-}\mu\text{m}$  thickness gold foil. The hot electrons were counted at the four boundaries of the square gold wire which located in the center of the gold foil from the PIC simulations. The hot electrons passed through the foil for one trip and produced secondary electrons and x-rays through bremsstrahlung and line radiation. The outgoing x-rays in the  $4\pi$  solid angle were counted to calculate the x-ray spectrum. In our Monte Carlo simulations, the initial distributions of hot electron energy and angle came from the PIC simulations, while the spatial distribution was assumed to be a point source.

Here we gave a brief discussion of the mechanism of hot electron relaxation, which was useful to understand the comparisons of hot electron-driven x-ray yield from Monte Carlo simulations with the time integrated experimental results. In general, the mechanism of the hot electron relaxation was quite complex in the solid density plasmas, which was caused by the combination of adiabatic cooling, electron-electron collision, electron-ion collision, plasma expansion, instabilities, and so on [43-45]. The processes of the plasma expansion and instabilities were naturally treated by the PIC simulations solving the particle equation of motion and Maxwell equations. But the collision was not included in our PIC simulations since we used a reduced density ( $5n_c$ ) to model the real density of gold for saving the computational time. However, the collisional effect was much weaker than the kinetic effect for such a reduced density and thus was reasonable to be ignored [46]. The hot electron spectra simulated by the PIC code, were then constitute to the input to the Monte Carlo code Geant4

simulations, which post-processed the electron collisions, the bremsstrahlung radiation and line emission in the target. Since the Monte Carlo simulations were a post-processing data analysis, the results were not fed back into the PIC. Ideally, one could couple PIC with Monte Carlo simulations and compute the x-ray yield self-consistently. It required to use the real density of gold and thus huge computational power, which will be investigated in our future work.

### III. SIMULATION RESULTS

#### A. Electrons energy distribution given by PIC

##### 1. Electrostatic sheath field and quasi-static magnetic field

Figure 3. The spatial distributions of the quasi-static electric fields  $E_x$ ,  $E_y$ , and quasi-static magnetic field  $B_z$  (averaged in one laser period), at  $\sim 4$  fs after the laser peak intensity hitting the target. The red dashed lines distinguished the main targets and the preplasmas. The red dashed line squares were the defined probe boxes (the probe boxes for the wire with or without a substrate were faded slightly to observe the fields more clearly).

The quasi-static electric and the magnetic fields confined the motion of the electrons and caused the electron recirculation [47-50]. To examine the influence of the substrate on the electron recirculation, the electrostatic field and the quasi-static magnetic field were shown in figure 3, which illustrated the spatial distributions of the maximal quasi-static electric and magnetic field at 4 fs after the laser peak intensity hitting the target. The sheath electric field  $E_x$  and the quasi-static magnetic field  $B_z$  at the rear surface had no observable difference between the thin foil and the wires with or without a substrate. The maximum values of  $E_x$  and  $B_z$  were 4–5 TV/m and 50–60 MG, respectively. For the three geometries, the  $E_x$  and  $B_z$  were markedly higher than those of the thick foil, which meant that the substrate had to be thin enough to maintain the electron recirculation, as was found in our previous work [39].

We noted that the FWHM pulse duration in our simulation was 600 fs, which meant that the relativistic laser has already interacted with the target for more than 300 fs, at  $\sim 4$  fs after the laser peak intensity. Since the thickness of the foil target was 10  $\mu\text{m}$ , it took  $\sim 30$  fs for relativistic electrons passing through the target and building up the electrostatic sheath field at rear. The recirculation effect occurred as soon as the sheath field created. From figure 3, it was shown that the longitudinal sheath electrostatic field was  $\sim 4$  TV/m with the scale length  $\sim 0.5$   $\mu\text{m}$ , which resulted in the sheath potential  $\sim 2$  MeV. The scale length of the electrostatic sheath field was given by the Debye length  $\lambda_D$  of the laser generated hot electrons, versus their density  $n_h$  and temperature  $T_h$ :  $\lambda_D = \sqrt{kT_h/4\pi e^2 n_h} \approx 2.35[\mu\text{m}]\sqrt{T_h[\text{MeV}]/n_h[10^{19}\text{cm}^{-3}]}$ . The hot electron temperature or mean kinetic energy  $T_h$  could be estimated by the ponderomotive scaling [35]  $T_h = (\sqrt{1 + a_0^2} - 1)m_e c^2 \approx 0.6$  MeV. The hot electron density  $n_h$  extracted from our simulation was  $\sim 0.1n_c$ , which was on the same order of our previous work [51]. Thus, we can estimate the Debye length of the hot electrons  $\lambda_D \approx 0.57$   $\mu\text{m}$ , which was very close to the scale length of the longitudinal sheath electrostatic field from the PIC simulations.

A fraction of the relativistic electrons with kinetic energy lower than the sheath potential re-entered the target pulled by the target normal sheath field. The reflux component was clearly seen from the phase space density, as shown in figure 2 from our previous work [51] even before the peak laser intensity hitting the target.

We clearly saw the difference of the transverse sheath electric field  $E_y$  and the azimuth quasi-static magnetic field  $B_z$  at the side surfaces, which were nearly zero in the thick and thin foils. While in the wire with a substrate, the  $E_y$  sheath electric

field appeared at the interface between the wire and the substrate. In the freestanding wire, the  $E_y$  sheath electric field was located around the critical density surface of the preplasmas. The Biermann battery effect [25] likely caused quasi-static magnetic fields  $B_z$  appeared at the same location as  $E_y$ . The maximum values of the electric and magnetic fields in the freestanding wire ( $E_y \sim 1.3$  TV/m,  $B_z \sim 190$  MG) were lower than that in the wire with substrate ( $E_y \sim 4.2$  TV/m,  $B_z \sim 260$  MG) probably due to the smoother density profile. However, the field ranges of the former were significantly larger. The enhancement in the sheath electric field and quasi-static magnetic field in the microwires modified the electron motion and the hard x-ray emission, which were discussed as following.

## 2. Electron energy spectra

Figure 4. Electron energy spectra ( $>50$  keV) counted at four boundaries of the probe boxes of the  $10 \mu\text{m} \times 10 \mu\text{m}$  gold wire in the PIC simulations. (a) center of the thick gold foil, (b) center of the thin gold foil, (c) gold wire with CH substrate, and (d) freestanding gold wire. The inset is an enlarged view of the low-energy range below 1.2 MeV. It was noticed that all the hot electron energy spectra shown in the paper were integrated during the entire simulation time, i.e., 2 ps.

When changing the target structure from foil to wire, the different sheath electric fields and the quasi-static magnetic fields around the target surfaces altered the electron acceleration. In this part, we showed the time-integrated hot electron energy spectra to explore the electron motion. We noticed that since the experiments typically measured the time integrated x-ray yield. To better compare with it from simulations, here all the hot electron energy spectra extracted from the PIC simulations were integrated during the entire simulation time, i.e., 2 ps, which were then coupled into the Geant4 for simulating the x-ray yield.

Firstly, we showed the hot electron energy spectra that crossed each boundary of the probe box for all the studied targets in figure 4. The significant difference was found at the front side of laser irradiation. It indicated the significant difference of the electron recirculation in the different target geometries. In the case of thick foil shown in figure 4(a), which had no sheath field at the rear surface and thus no electron recirculation, the laser accelerated electrons traversed through the target for only one trip. The electrons were accelerated mainly by the laser Lorentz force component and moved forward along the laser direction of  $45^\circ$ . Therefore, the electrons mainly traversed through the right and up boundaries of the probe box with similar energy spectra. The spectra showed at least two temperature components of electrons (here we named them the “hotter” and “colder” components) following bi-Maxwellian distribution with the transition energy at around 1 MeV. For the thin foil shown in figure 4(b), the electrons traversed to the rear surface of the target and then reflected back to the target by the longitudinal electrostatic sheath, and re-accelerated by the laser field at the front surface. Hence, the “colder” electron component ( $<1$ MeV) across the right boundary was less than that of the other three boundaries, which also held on for the wire target. In contrast, the “hotter” electron component ( $>1$ MeV) crossing the right boundary of the probe box was enhanced significantly, and also for the left and up boundaries. The “hotter” electron component across the down surface was the weakest one in the thin foil. When changed to the wire target, the additional confinement fields along the y-direction further enhanced the electron recirculation. Therefore the “hotter” electrons component was raised significantly at the down surface of the wire, and became more isotropic in the four boundaries, as shown in figure 4 (c) and (d). In the case of the freestanding wire, the four boundaries have almost identical energy spectra for the “hotter” component, while the “colder” electron component across the right and up boundaries was weakened.

Figure 5. (a) Number and (b) mean kinetic energy of electrons crossing each surface of the square probe box of the gold wire with different geometries: 1) center of thick foil; 2) center of thin foil; 3) wire with a substrate and 4) freestanding wire.

Secondly, we noted that the “hotter” electron component was continuously increased from thick foil, to thin foil, and finally to freestanding wire with the electron recirculation enhancement, while the “colder” component was decreasing. To understand it more clearly, we calculated the electron number, and the mean energy for all the studied target as shown in figure 5. It was observed that the total number of electrons and mean energy continuously enhanced from thick foil to finally freestanding wire with 4 times increment in the mean kinetic energy and 1.7 times enhancement in the total electron number. In particular, from the wire with substrate to freestanding wire, the electrons number was only increased slightly, but the hot electron temperature enhanced markedly which was further discussed in the following section.

Figure 6 Total electron energy distributions (>50 keV) that summed all of the electrons counted at the four surfaces of the probe box. The insert shows the enlarged view of the low-energy range. It is noticed that all the hot electron energy spectra shown in the paper were integrated during the entire simulation time, i.e., 2 ps.

Finally, we show the total electron energy spectra of four kinds of target in figure 6, which is the summed up of the electron spectra across the four boundaries of the probe box in figure 4. The electron acceleration mechanism in the picoseconds laser pulse irradiated large-scale pre-plasma differed to the conventional ponderomotive mechanism. In the case of picosecond pulse irradiation, the “super-ponderomotive” electrons with movement exceeding the ponderomotive movement limit of  $m_e c a_0^2 / 2$  was typically observed, which was attributed to the stochastic heating [52, 53], or direct laser acceleration [54]. Even without initial preplasmas, the plasma expansion in picosecond duration also caused under-dense plasma and energetic electrons [55]. In this case, the light pressure swept off the preformed plasma and steepened the density gradient, which shortened the acceleration distance and reduced the slope temperature by the JxB acceleration [56, 57]. Besides the oscillating term (AC), the DC-ponderomotive force could also produce another component of low-energy electrons at the steep interface [58]. Therefore, the hot electron spectra exhibited several slope temperatures. The absorption mechanisms and electron slope temperatures were time-dependent [58, 59], which sensitively relied on the laser duration, laser intensity, plasma profile, and electron recirculation [60] etc. Thus, several characteristic temperatures in our simulation were predicted using the peak laser intensity of  $a = 1.88$ : the ponderomotive scaling  $T_{pond} = (\gamma - 1)m_e c^2 \sim 600\text{keV}$  generated near the critical density[35], the reduced ponderomotive scaling  $T_{pond}^r = (\gamma - 1)m_e c^2 (n_p / \gamma n_c)^{0.5} \sim 160\text{keV}$  by JxB at steep interface ( $n_p = 8a^2 n_c$ ) [56, 57, 61], the DC-ponderomotive scaling  $T_{DC} \sim 30\text{-}450\text{keV}$  depending on maximal density[58], and the super-ponderomotive temperature  $T_h \sim$  several MeV produced in under-dense plasma [53, 56, 62, 63]. As seen from our simulations in figure 6, the thick foil exhibited three slope temperatures: cold temperature  $T_c \sim 120\text{keV}$ , moderate temperature  $T_m \sim 760\text{keV}$ , and hot temperature  $T_h \sim 2.6\text{MeV}$ , which matched to the reduced or DC-ponderomotive scaling, the ponderomotive scaling, and the super-ponderomotive temperature respectively.

Electron recirculation in thin foil and wires raised the slope temperatures of electrons, as seen in figure 6. The spanning range of the moderate temperature corresponding to the ponderomotive scaling diminished from thick foil to freestanding wire. The transition point between the cold and moderate temperatures moved from 600 keV (thick foil), to 1 MeV (thin foil), and  $\sim 2$  MeV for wire target, which was attributed to the electron recirculation [60]. In all the target geometries, the cold ( $T_c$ ) and hot ( $T_h$ ) temperatures were different: the former increased from  $T_c \sim 120\text{keV}$  (thick foil), to  $T_c \sim 200\text{keV}$



(thin foil), and to  $T_c \sim 670\text{keV}$  (both wires); and the latter was very close at  $T_h \sim 2.6\text{MeV}$  from thick foil to wire with substrate, but increase to  $T_h \sim 3.6\text{MeV}$  for freestanding wire.

Although both of the cold and hot electrons components hardened from thick to finally freestanding wire, different behavior exhibited at the electrons number in the lower and higher energy electrons groups. The number of lower energy electrons in the range of 70 - 900keV continued to decay from thick foil to freestanding wire. While the number of higher energy electrons increased significantly on the contrary. It indicated that the electron recirculation re-injected into the laser field that stochastically accelerated the electron to super-ponderomotive energy. This process converted the cold electrons to hot electrons.

For the wire target that we focused here, it showed that the substrate had no observable influence on the low energy electrons below 900keV, at which range the lower energy electrons was only slightly decreased without substrate. But the higher energy electrons above 900 keV was markedly enhanced without substrate. The turning point was shifted from 900 keV to 270 keV if increasing the density of the substrate close to that of the wire, which was the case of thin foil. Therefore the density of the substrate should be as low as possible to minimize its influence on the electron generation and x-ray emission.

## B. Hard x-ray emission calculated by MC

Electron motions crossing the four boundaries of the square probe box of the gold wire with all the studied geometries, including the energy and angular distributions obtained by PIC simulation, were coupled into the Monte Carlo code Geant4 to simulate the x-rays emission from a 10- $\mu\text{m}$  Au target. The angularly integrated x-ray spectra in the  $4\pi$  solid angles for the four kinds of targets were discussed as following.

Figure 7. Angularly integrated x-ray spectra from 10 keV to 20 MeV emitted by 10  $\mu\text{m}$   $\times$  10  $\mu\text{m}$  square gold wire for four kinds of targets calculated by Monte Carlo simulations. The insert showed the enlarged view of the low-energy range.

### 1. MeV gamma ray

Figure 7 showed the simulated x-rays spectra emitted from the 10  $\mu\text{m}$   $\times$  10  $\mu\text{m}$  square gold wire in the range from 10 keV to 20 MeV. The insert showed the enlarged view in the low-energy range from 10 keV to 200 keV. As observed, the hard x-ray spectra also exhibited two-slope temperature distribution, similar to that of the hot electron spectra shown in figure 6. Although the electron energy spectra for the cold and hot components exhibited different scaling to the target geometry, the x-ray spectra presented the same trend in the entire range from 50keV to 20MeV when altering the electron recirculation. The freestanding wire radiated the strongest hard x-ray in the range of 50 keV-20 MeV, followed by the wire with a substrate, the wire buried in equal-density thin foil, and the wire buried in equal-density thick foil. The difference of x-ray intensity among the targets became significantly toward the harder x-ray range of MeV. The radiation intensity ratio for the different targets were 9.8: 6.3: 3.1: 1 at 1 MeV, and sharply increased to 22: 6.6: 3.6: 1 at 5 MeV. Thus, for the application of gamma-ray radiography using the  $\sim\text{MeV}$  photons, the freestanding wire was best choice. The substrate largely suppressed the MeV gamma ray emission and had to be avoided in the gamma-ray radiography experiment.

### 2. 10–200 keV hard x-ray emission for Compton radiography of implosion capsule

The influence of low-Z substrate could be ignored in the 10–200 keV x-ray range for the application of Compton radiography in the ICF implosion capsule. As shown in the insert of figure 7, the intensity ratio decayed to a minimal value of 1.9: 1.8: 1.3: 1 at 100 keV. The wires still produced higher hard x-ray emission with a factor of 2 higher than that buried in foils, including the  $K_{\alpha}$ ,  $K_{\beta}$ , and L-band characteristic lines and bremsstrahlung continuum emission. However, the wires with or without a substrate had no observable different x-ray spectra in the low energy range, which was consistent to that the substrate had no observable influence on the low energy electrons with kinetic energy less than 900keV as discussed above. It indicated that a CH thin substrate could be attached to the wire to ease the target fabrication and experimental performance to radiate 10–200 keV hard x-ray emission for Compton radiography. The density of the substrate should be low enough, at least lower than that of the wire.

The x-ray spectra had smaller slope temperatures than electron spectra in all the studied cases. It showed that the x-ray slope temperatures of thick foil were decreased to  $T_c \sim 100$  keV and  $T_h \sim 1.6$  MeV, compared to the electron temperatures of  $T_c \sim 120$  keV,  $T_m \sim 760$  keV, and  $T_h \sim 2.6$  MeV. The freestanding wire also exhibited lower temperatures the in x-ray spectrum, which were  $T_c \sim 340$  keV and  $T_h \sim 2.3$  MeV vs the electron temperatures of  $T_c \sim 670$  keV and  $T_h \sim 3.6$  MeV. The softened x-ray spectra was caused by the incomplete energy deposition of hot electrons when traversing through the gold target. Only a small fraction of electron energy was deposited and converted to x-ray. The relation of the x-ray spectrum and the electron kinetic energy spectra could be derived from an analytic formula [64].

Figure 8. Simulation (red triangles) and experimental (black squares) results for the conversion efficiency (CE) from the laser energy to the hard x-ray emission. (a) 70–200 keV, and (b) 100–200 keV. The red dashed lines indicate a fit for the experimental data with a power function that relates the CEs to the laser intensities.

Finally, we compared our simulation results with the previous experiments in terms of the conversion efficiency (CE) from the laser energy to the hard x-ray emission in the ranges of 70–200 keV [5] and 100–200 keV [40] in the case of gold wire target, as shown in figure 8. In the experiments, 10- $\mu$ m diameter gold wires with substrates of 10- $\mu$ m CH or 5- $\mu$ m Al were irradiated by an intense picosecond lasers pulse. It was shown that the simulation results were agreed well with the experimental results. In the application of Compton radiography of the implosion capsule with 70–200 keV x-rays, the gold wire with a substrate had very close CE as the freestanding wire (about  $10^{-3}$  for  $CE_{70-200}$  and  $8 \times 10^{-4}$  for  $CE_{100-200}$ ). The CEs of the wires w/o a substrate were 1–2 times of those for the wires buried in thin foil (about  $7 \times 10^{-4}$  for  $CE_{70-200}$  and  $5 \times 10^{-4}$  for  $CE_{100-200}$ ) and 2–3 times of those for the wires buried in thick foil (about  $5 \times 10^{-4}$  for  $CE_{70-200}$  and  $3 \times 10^{-4}$  for  $CE_{100-200}$ ).

It was worthy to point that the hot electrons continued to produce the energetic x-ray source before the relaxation, while it was experimentally measured that the thermalization of fast electrons occurred over time scales on the order of 10 ps [44], which was much longer than our simulation time 2 ps. Thus, ignoring the long time evolution of the hot electron distribution underestimated the energetic x-ray yield when comparing to the experimental results. But the influence of electron relaxation decayed rapidly toward harder x-ray range, and the duration of hard x-ray pulse of > 70keV was considered typically close to the laser pulse duration [4, 5, 7].

## VI. CONCLUSION

We explored the influence of a thin CH substrate on a gold microwire to radiate the point hard x-ray source driven by a picosecond laser pulse via PIC and Monte Carlo simulations. The gold wires with or without a thin CH substrate produced more intense hard x-ray emissions than the equal-volume radiator buried in foils from 10 keV to tens of MeV due to the electron recirculation. The electron recirculation also enhanced the MeV gamma ray emitted from the freestanding wire

with a factor of several times, compared to the wire with a substrate, while the gain decayed toward the softer x-ray. For the x-ray photons in the range of 70–200 keV which was typically used in the Compton radiography of the ICF implosion target, the thin CH substrate had no observable influence on the x-ray emission from the gold wire. The simulation results agreed with the previous experimental results. Valuable suggestions for experimental design could be given based on those results: the substrate should be low-Z (low-density and low atomic number) and thin enough to avoid x-ray noise and enhance the electron recirculation and thus Bremsstrahlung radiation. Freestanding gold wire is preferred for a MeV gamma ray point source, while the gold wire with a 10- $\mu\text{m}$  CH substrate can be used for the  $\sim 100$  keV x-ray Compton radiography of an ICF implosion target to ease the target fabrication and experimental performance.

#### ACKNOWLEDGEMENT

This work was supported by the Strategic Priority Research Program of Chinese Academy of Sciences (Grant No. XDB16000000), the National Natural Science Foundation of China (Grant Nos. 11775223, 11375197, 11605200, and 11275202), the Science Challenge Project (Grant No. TZ2016005), the Open Fund of the State Key Laboratory of High Field Laser Physics (SIOM), and the Fundamental Research Funds for the Central Universities.

#### DATA AVAILABILITY STATEMENT

The data that supports the findings of this study are available within the article [and its supplementary material].

#### REFERENCE

1. S. Atzeni and J. Meyer-ter-Vehn, *The Physics of Inertial Fusion: Beam Plasma Interaction, Hydrodynamics, Hot Dense Matter*. (OUP Oxford, 2004).
2. J. R. Rygg, O. S. Jones, J. E. Field, M. A. Barrios, L. R. Benedetti, G. W. Collins, D. C. Eder, M. J. Edwards, J. L. Kline, J. J. Kroll, O. L. Landen, T. Ma, A. Pak, J. L. Peterson, K. Raman, R. P. Town and D. K. Bradley, *Phys Rev Lett* **112** (19), 195001 (2014).
3. M. A. Barrios, S. P. Regan, K. B. Fournier, R. Epstein, R. Smith, A. Lazicki, R. Rygg, D. E. Fratanduono, J. Eggert, H. S. Park, C. Huntington, D. K. Bradley, O. L. Landen and G. W. Collins, *Rev Sci Instrum* **85** (11), 11D502 (2014).
4. R. Tommasini, A. MacPhee, D. Hey, T. Ma, C. Chen, N. Izumi, W. Unites, A. MacKinnon, S. P. Hatchett, B. A. Remington, H. S. Park, P. Springer, J. A. Koch, O. L. Landen, J. Seely, G. Holland and L. Hudson, *Rev Sci Instrum* **79** (10), 10E901 (2008).
5. R. Tommasini, S. P. Hatchett, D. S. Hey, C. Iglesias, N. Izumi, J. A. Koch, O. L. Landen, A. J. MacKinnon, C. Sorce, J. A. Delettrez, V. Y. Glebov, T. C. Sangster and C. Stoeckl, *Phys Plasmas* **18** (5), 056309 (2011).
6. H. Chen, M. R. Hermann, D. H. Kalantar, D. A. Martinez, P. Di Nicola, R. Tommasini, O. L. Landen, D. Alessi, M. Bowers, D. Browning, G. Brunton, T. Budge, J. Crane, J. M. Di Nicola, T. Doppner, S. Dixit, G. Erbert, B. Fishler, J. Halpin, M. Hamamoto, J. Heebner, V. J. Hernandez, M. Hohenberger, D. Homoelle, J. Honig, W. Hsing, N. Izumi, S. Khan, K. LaFortune, J. Lawson, S. R. Nagel, R. A. Negres, L. Novikova, C. Orth, L. Pelz, M. Prantil, M. Rushford, M. Shaw, M. Sherlock, R. Sigurdsson, P. Wegner, C. Widmayer, G. J. Williams, W. Williams, P. Whitman and S. Yang, *Phys Plasmas* **24** (3), 033112 (2017).
7. R. Tommasini, C. Bailey, D. K. Bradley, M. Bowers, H. Chen, J. M. Di Nicola, P. Di Nicola, G. Gururangan, G. N. Hall, C. M. Hardy, D. Hargrove, M. Hermann, M. Hohenberger, J. P. Holder, W. Hsing, N. Izumi, D. Kalantar, S. Khan, J. Kroll, O. L. Landen, J. Lawson, D. Martinez, N. Masters, J. R. Nafziger, S. R. Nagel, A. Nikroo, J. Okui, D. Palmer, R. Sigurdsson, S. Vohnhof, R. J. Wallace and T. Zobrist, *Phys Plasmas* **24** (5), 053104 (2017).

This is the author's peer reviewed, accepted manuscript. However, the online version of record will be different from this version once it has been copyedited and typeset.

PLEASE CITE THIS ARTICLE AS DOI: 10.1063/1.50023189

8. A. Morace, L. Fedeli, D. Batani, S. Baton, F. N. Beg, S. Hulin, L. C. Jarrott, A. Margarit, M. Nakai, M. Nakatsutsumi, P. Nicolai, N. Piovella, M. S. Wei, X. Vaisseau, L. Volpe and J. J. Santos, *Phys Plasmas* **21** (10), 102712 (2014).
9. E. Brambrink, H. G. Wei, B. Barbrel, P. Audebert, A. Benuzzi-Mounaix, T. Boehly, T. Endo, C. D. Gregory, T. Kimura, R. Kodama, N. Ozaki, H. S. Park and M. Koenig, *Phys Rev E Stat Nonlin Soft Matter Phys* **80** (5 Pt 2), 056407 (2009).
10. E. Brambrink, H. G. Wei, B. Barbrel, P. Audebert, A. Benuzzi-Mounaix, T. Boehly, T. Endo, C. Gregory, T. Kimura, R. Kodama, N. Ozaki, H. S. Park, M. R. le Gaohec and M. Koenig, *Phys Plasmas* **16** (3), 033101 (2009).
11. H. Sawada, S. Lee, T. Shiroto, H. Nagatomo, Y. Arikawa, H. Nishimura, T. Ueda, K. Shigemori, A. Sunahara, N. Ohnishi, F. N. Beg, W. Theobald, F. Pérez, P. K. Patel and S. Fujioka, *Appl Phys Lett* **108** (25), 254101 (2016).
12. L. C. Jarrott, A. J. Kemp, L. Divol, D. Mariscal, B. Westover, C. McGuffey, F. N. Beg, M. Suggit, C. Chen, D. Hey, B. Maddox, J. Hawreliak, H. S. Park, B. Remington, M. S. Wei and A. MacPhee, *Phys Plasmas* **21** (3), 031211 (2014).
13. K. Vaughan, A. S. Moore, V. Smalyuk, K. Wallace, D. Gate, S. G. Glendinning, S. McAlpin, H. S. Park, C. Sorce and R. M. Stevenson, *High Energy Density Physics* **9** (3), 635-641 (2013).
14. G. Hu, X. Zhang, J. Zheng, A. Lei, B. Shen, Z. Xu, J. Zhang, J. Yang, G. Yang, M. Wei, J. Li and Y. Ding, *Plasma Science and Technology* **14** (10), 864-870 (2012).
15. B. R. Maddox, H. S. Park, B. A. Remington, C. Chen, S. Chen, S. T. Prisbrey, A. Comley, C. A. Back, C. Szabo, J. F. Seely, U. Feldman, L. T. Hudson, S. Seltzer, M. J. Haugh and Z. Ali, *Phys Plasmas* **18** (5), 056709 (2011).
16. A. Kritcher, P. Neumayer, C. Brown, P. Davis, T. Döppner, R. Falcone, D. Gericke, G. Gregori, B. Holst and O. Landen, *Physical review letters* **103** (24), 245004 (2009).
17. H. S. Park, D. M. Chambers, H. K. Chung, R. J. Clarke, R. Eagleton, E. Giraldez, T. Goldsack, R. Heathcote, N. Izumi, M. H. Key, J. A. King, J. A. Koch, O. L. Landen, A. Nikroo, P. K. Patel, D. F. Price, B. A. Remington, H. F. Robey, R. A. Snavely, D. A. Steinman, R. B. Stephens, C. Stoeckl, M. Storm, M. Tabak, W. Theobald, R. P. J. Town, J. E. Wickersham and B. B. Zhang, *Phys Plasmas* **13** (5), 056309 (2006).
18. L. M. Chen, P. Forget, S. Fourmaux, J. C. Kieffer, A. Krol, C. C. Chamberlain, B. X. Hou, J. Nees and G. Mourou, *Phys Plasmas* **11** (9), 4439-4445 (2004).
19. H. S. Park, B. R. Maddox, E. Giraldez, S. P. Hatchett, L. T. Hudson, N. Izumi, M. H. Key, S. Le Pape, A. J. MacKinnon, A. G. MacPhee, P. K. Patel, T. W. Phillips, B. A. Remington, J. F. Seely, R. Tommasini, R. Town, J. Workman and E. Brambrink, *Phys Plasmas* **15** (7), 072705 (2008).
20. O. Klein and Y. Nishina, *Zeitschrift für Physik* **52** (11-12), 853-868 (1929).
21. B. R. Maddox, H. S. Park, B. A. Remington, N. Izumi, S. Chen, C. Chen, G. Kimminau, Z. Ali, M. J. Haugh and Q. Ma, *Rev Sci Instrum* **82** (2), 023111 (2011).
22. H. U. I. Chen and S. C. Wilks, *Laser and Particle Beams* **23** (4), 411-416 (2005).
23. T. Ceccotti, A. Levy, H. Popescu, F. Reau, P. D'Oliveira, P. Monot, J. P. Geindre, E. Lefebvre and P. Martin, *Phys Rev Lett* **99** (18), 185002 (2007).
24. S. Buffechoux, J. Psikal, M. Nakatsutsumi, L. Romagnani, A. Andreev, K. Zeil, M. Amin, P. Antici, T. Burris-Mog, A. Compant-La-Fontaine, E. d'Humieres, S. Fourmaux, S. Gaillard, F. Gobet, F. Hannachi, S. Kraft, A. Mancic, C. Plaisir, G. Sarri, M. Tarisien, T. Toncian, U. Schramm, M. Tampo, P. Audebert, O. Willi, T. E. Cowan, H. Pepin, V. Tikhonchuk, M. Borghesi and J. Fuchs, *Phys Rev Lett* **105** (1), 015005 (2010).
25. B. Albertazzi, S. N. Chen, P. Antici, J. Boker, M. Borghesi, J. Breil, V. Dervieux, J. L. Feugeas, L. Lancia, M. Nakatsutsumi, P. Nicolai, L. Romagnani, R. Shepherd, Y. Sentoku, M. Starodubtsev, M. Swantusch, V. T. Tikhonchuk, O. Willi, E. d'Humie`res, H. Pepin and J. Fuchs, *Phys. Plasmas* **22**, 123108 (2015).
26. L. G. Huang, H.-P. Schlenvoigt, H. Takabe and T. E. Cowan, *Phys Plasmas* **24**, 103115 (2017).
27. J. Myatt, W. Theobald, J. A. Delettrez, C. Stoeckl, M. Storm, T. C. Sangster, A. V. Maximov and R. W. Short, *Phys Plasmas* **14** (5), 056301 (2007).

This is the author's peer reviewed, accepted manuscript. However, the online version of record will be different from this version once it has been copyedited and typeset.

PLEASE CITE THIS ARTICLE AS DOI: 10.1063/5.0023189

28. P. Neumayer, B. Aurand, M. Basko, B. Ecker, P. Gibbon, D. C. Hochhaus, A. Karmakar, E. Kazakov, T. Kühl, C. Labaune, O. Rosmej, A. Tauschwitz, B. Zielbauer and D. Zimmer, *Phys Plasmas* **17** (10), 103103 (2010).
29. P. M. Nilson, W. Theobald, J. Myatt, C. Stoeckl, M. Storm, O. V. Gotchev, J. D. Zuegel, R. Betti, D. D. Meyerhofer and T. C. Sangster, *Phys Plasmas* **15** (5), 056308 (2008).
30. M. N. Quinn, X. H. Yuan, X. X. Lin, D. C. Carroll, O. Tresca, R. J. Gray, M. Coury, C. Li, Y. T. Li, C. M. Brenner, A. P. L. Robinson, D. Neely, B. Zielbauer, B. Aurand, J. Fils, T. Kuehl and P. McKenna, *Plasma Physics and Controlled Fusion* **53** (2), 025007 (2011).
31. H. Sawada, M. S. Wei, S. Chawla, A. Morace, K. Akli, T. Yabuuchi, N. Nakanii, M. H. Key, P. K. Patel, A. J. Mackinnon, H. S. McLean, R. B. Stephens and F. N. Beg, *Phys Rev E Stat Nonlin Soft Matter Phys* **89** (3), 033105 (2014).
32. W. Theobald, K. Akli, R. Clarke, J. A. Delettrez, R. R. Freeman, S. Glenzer, J. Green, G. Gregori, R. Heathcote, N. Izumi, J. A. King, J. A. Koch, J. Kuba, K. Lancaster, A. J. MacKinnon, M. Key, C. Mileham, J. Myatt, D. Neely, P. A. Norreys, H. S. Park, J. Pasley, P. Patel, S. P. Regan, H. Sawada, R. Shepherd, R. Snavely, R. B. Stephens, C. Stoeckl, M. Storm, B. Zhang and T. C. Sangster, *Phys Plasmas* **13** (4), 043102 (2006).
33. A. Compant La Fontaine, C. Courtois, E. Lefebvre, J. L. Bourgade, O. Landoas, K. Thorp and C. Stoeckl, *Phys Plasmas* **20** (12), 123111 (2013).
34. M. Makita, G. Nersisyan, K. McKeever, T. Dzelzainis, S. White, B. Kettle, B. Dromey, D. Doria, M. Zepf, C. L. S. Lewis, A. P. L. Robinson, S. B. Hansen and D. Riley, *Phys Plasmas* **21** (2), 023113 (2014).
35. S. C. Wilks, W. L. Kruer, M. Tabak and A. B. Langdon, *Phys Rev Lett* **69** (9), 1383-1386 (1992).
36. A. Pukhov and J. Meyer-ter-Vehn, *Physics of Plasmas* **5** (5), 1880-1886 (1998).
37. K. McKeever, M. Makita, G. Nersisyan, T. Dzelzainis, S. White, B. Kettle, B. Dromey, M. Zepf, G. Sarri, D. Doria, H. Ahmed, C. L. Lewis, D. Riley and A. P. Robinson, *Phys Rev E Stat Nonlin Soft Matter Phys* **91** (3), 033107 (2015).
38. S. R. Nagel, H. Chen, J. Park, M. Foord, A. U. Hazi, T. J. Hillsabeck, S. M. Kerr, E. V. Marley and G. J. Williams, *Appl Phys Lett* **110** (14), 144102 (2017).
39. M. Li, G.-y. Hu, L. Huang and J. Zheng, *Plasma Physics and Controlled Fusion* **62**, 095006 (2020).
40. R. Tommasini, S. P. Hatchett, N. Izumi, Jeffrey A. Koch, H.-S. Park, B. Maddox, B. Remington, Andy MacKinnon, A. MacPhee, D. Hey, W. Unites, M. Key and O. Landen, *Development of backlighting sources for a Compton Radiography diagnostic of Inertial Confinement Fusion targets: interim pro-gress report, LLNL-TR-429373*. (2010).
41. Y. Sentoku and A. J. Kemp, *Journal of Computational Physics* **227** (14), 6846-6861 (2008).
42. S. Agostinelli, J. Allison, K. Amako, J. Apostolakis, H. Araujo, P. Arce, M. Asai, D. Axen, S. Banerjee, G. Barrand, F. Behner, L. Bellagamba, J. Boudreau, L. Broglia, A. Brunengo, H. Burkhardt, S. Chauvie, J. Chuma, R. Chytracsek, G. Cooperman, G. Cosmo, P. Degtyarenko, A. Dell'Acqua, G. Depaola, D. Dietrich, R. Enami, A. Feliciello, C. Ferguson, H. Fesefeldt, G. Folger, F. Foppiano, A. Forti, S. Garelli, S. Giani, R. Giannitrapani, D. Gibin, J. J. Gómez Cadenas, I. González, G. Gracia Abril, G. Greeniaus, W. Greiner, V. Grichine, A. Grossheim, S. Guatelli, P. Gumplinger, R. Hamatsu, K. Hashimoto, H. Hasui, A. Heikkinen, A. Howard, V. Ivanchenko, A. Johnson, F. W. Jones, J. Kallenbach, N. Kanaya, M. Kawabata, Y. Kawabata, M. Kawaguti, S. Kelner, P. Kent, A. Kimura, T. Kodama, R. Kokoulin, M. Kossov, H. Kurashige, E. Lamanna, T. Lampén, V. Lara, V. Lefebvre, F. Lei, M. Liendl, W. Lockman, F. Longo, S. Magni, M. Maire, E. Medernach, K. Minamimoto, P. Mora de Freitas, Y. Morita, K. Murakami, M. Nagamatu, R. Nartallo, P. Nieminen, T. Nishimura, K. Ohtsubo, M. Okamura, S. O'Neale, Y. Oohata, K. Paech, J. Perl, A. Pfeiffer, M. G. Pia, F. Ranjard, A. Rybin, S. Sadilov, E. Di Salvo, G. Santin, T. Sasaki, N. Savvas, Y. Sawada, S. Scherer, S. Sei, V. Sirotenko, D. Smith, N. Starkov, H. Stoecker, J. Sulkimo, M. Takahata, S. Tanaka, E. Tcherniaev, E. Safai Tehrani, M. Tropeano, P. Truscott, H. Uno, L. Urban, P. Urban, M. Verderi, A. Walkden, W. Wander, H. Weber, J. P. Wellisch, T. Wenaus, D. C. Williams, D. Wright, T. Yamada, H. Yoshida and D. Zschesche,

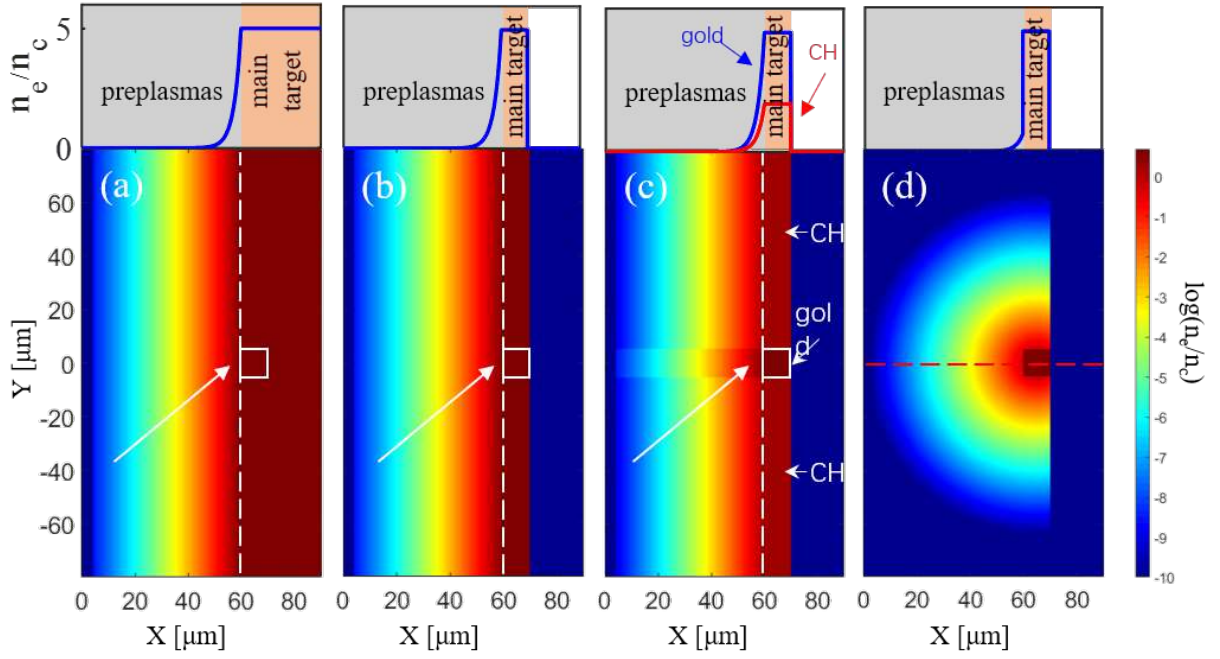
This is the author's peer reviewed, accepted manuscript. However, the online version of record will be different from this version once it has been copyedited and typeset.

PLEASE CITE THIS ARTICLE AS DOI: 10.1063/1.50023189

- Nuclear Instruments and Methods in Physics Research Section A: Accelerators, Spectrometers, Detectors and Associated Equipment **506** (3), 250-303 (2003).
43. Y. Sentoku, K. Mima, P. Kaw and K. Nishikawa, Physical Review Letters **90** (15), 155001 (2003).
  44. H. Chen, R. Shepherd, H. K. Chung, A. Kemp, S. B. Hansen, S. C. Wilks, Y. Ping, K. Widmann, K. B. Fournier, G. Dyer, A. Faenov, T. Pikuz and P. Beiersdorfer, Physical Review E **76** (5), 056402 (2007).
  45. B. Borm, D. Khaghani and P. Neumayer, Phys Plasmas **26** (2), 023109 (2019).
  46. A. J. Kemp, Y. Sentoku, V. Sotnikov and S. C. Wilks, Physical Review Letters **97** (23), 235001 (2006).
  47. B. Ramakrishna, S. Kar, A. P. Robinson, D. J. Adams, K. Markey, M. N. Quinn, X. H. Yuan, P. McKenna, K. L. Lancaster, J. S. Green, R. H. Scott, P. A. Norreys, J. Schreiber and M. Zepf, Phys Rev Lett **105** (13), 135001 (2010).
  48. G. Y. Hu, A. L. Lei, J. W. Wang, L. G. Huang, W. T. Wang, X. Wang, Y. Xu, B. F. Shen, J. S. Liu, W. Yu, R. X. Li and Z. Z. Xu, Phys Plasmas **17** (8), 083102 (2010).
  49. S. Kar, A. P. Robinson, D. C. Carroll, O. Lundh, K. Markey, P. McKenna, P. Norreys and M. Zepf, Phys Rev Lett **102** (5), 055001 (2009).
  50. Y. T. Li, X. H. Yuan, M. H. Xu, Z. Y. Zheng, Z. M. Sheng, M. Chen, Y. Y. Ma, W. X. Liang, Q. Z. Yu, Y. Zhang, F. Liu, Z. H. Wang, Z. Y. Wei, W. Zhao, Z. Jin and J. Zhang, Phys Rev Lett **96** (16), 165003 (2006).
  51. L. G. Huang, T. Kluge and T. E. Cowan, Phys Plasmas **23** (6), 063112 (2016).
  52. B. S. Paradkar, M. S. Wei, T. Yabuuchi, R. B. Stephens, M. G. Haines, S. I. Krasheninnikov and F. N. Beg, Phys Rev E Stat Nonlin Soft Matter Phys **83** (4 Pt 2), 046401 (2011).
  53. A. Sorokovikova, A. V. Arefiev, C. McGuffey, B. Qiao, A. P. Robinson, M. S. Wei, H. S. McLean and F. N. Beg, Phys Rev Lett **116** (15), 155001 (2016).
  54. A. G. Krygier, D. W. Schumacher and R. R. Freeman, Phys Plasmas **21** (2), 023112 (2014).
  55. A. J. Kemp and L. Divol, Phys Rev Lett **109** (19), 195005 (2012).
  56. A. J. Kemp, Y. Sentoku and M. Tabak, Phys Rev Lett **101** (7), 075004 (2008).
  57. A. J. Kemp, Y. Sentoku and M. Tabak, Phys Rev E Stat Nonlin Soft Matter Phys **79** (6 Pt 2), 066406 (2009).
  58. R. Mishra, Y. Sentoku and A. J. Kemp, Phys Plasmas **16** (11), 112704 (2009).
  59. J. Kim, A. J. Kemp, S. C. Wilks, D. H. Kalantar, S. Kerr, D. Mariscal, F. N. Beg, C. McGuffey and T. Ma, Phys Plasmas **25** (8), 083109 (2018).
  60. N. Iwata, Y. Sentoku, T. Sano and K. Mima, Nuclear Fusion **59** (8), 086035 (2019).
  61. N. Iwata, S. Kojima, Y. Sentoku, M. Hata and K. Mima, Nat Commun **9** (1), 623 (2018).
  62. B. Chrisman, Y. Sentoku and A. J. Kemp, Phys Plasmas **15** (5), 056309 (2008).
  63. N. Iwata, K. Mima, Y. Sentoku, A. Yogo, H. Nagatomo, H. Nishimura and H. Azechi, Phys Plasmas **24** (7), 073111 (2017).
  64. G. H. McCall, Journal of Physics D: Applied Physics **15** (5), 823-831 (1982).

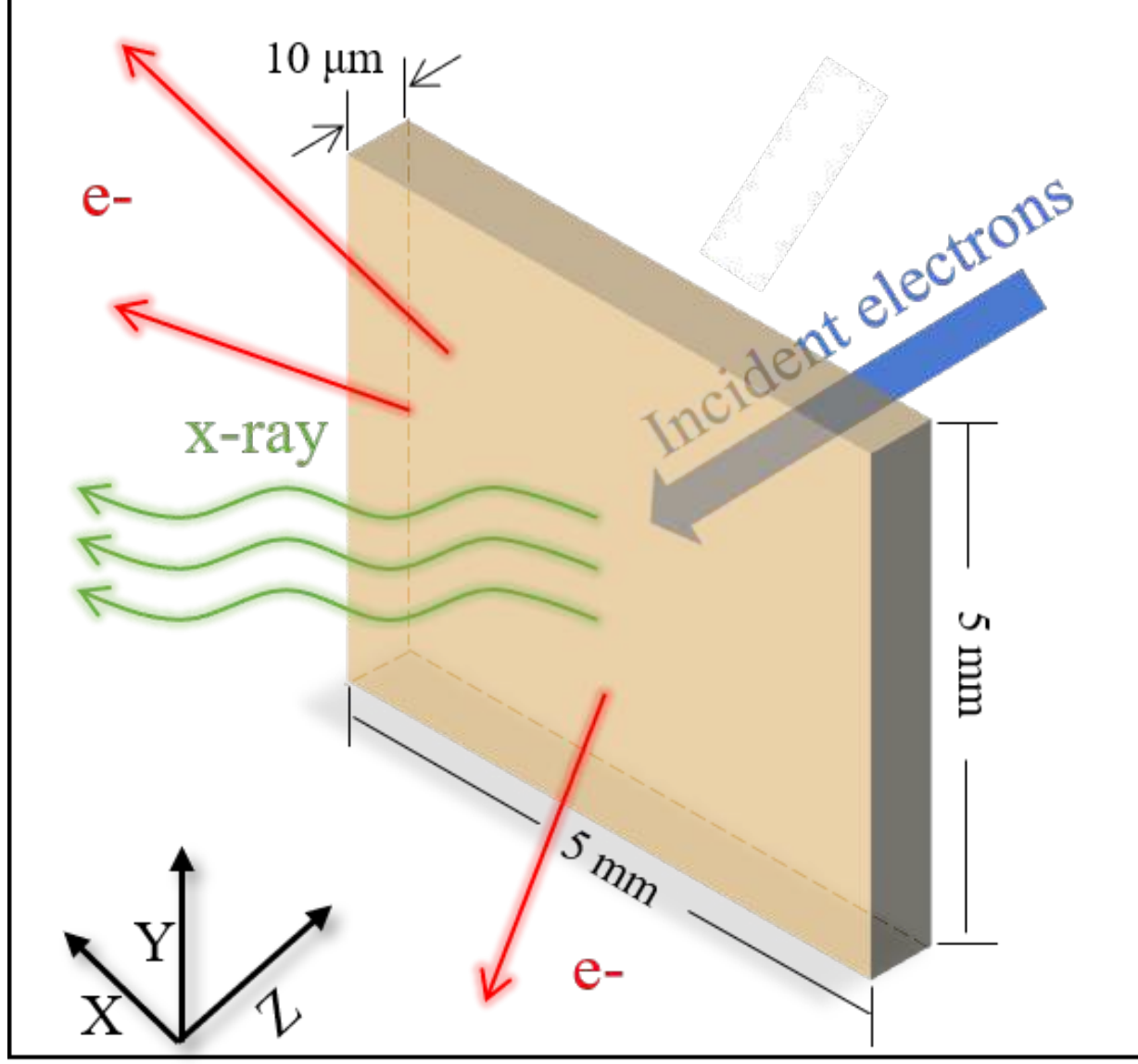
This is the author's peer reviewed, accepted manuscript. However, the online version of record will be different from this version once it has been copyedited and typeset.

PLEASE CITE THIS ARTICLE AS DOI: 10.1063/1.50023189



This is the author's peer reviewed, accepted manuscript. However, the online version of record will be different from this version once it has been copyedited and typeset.

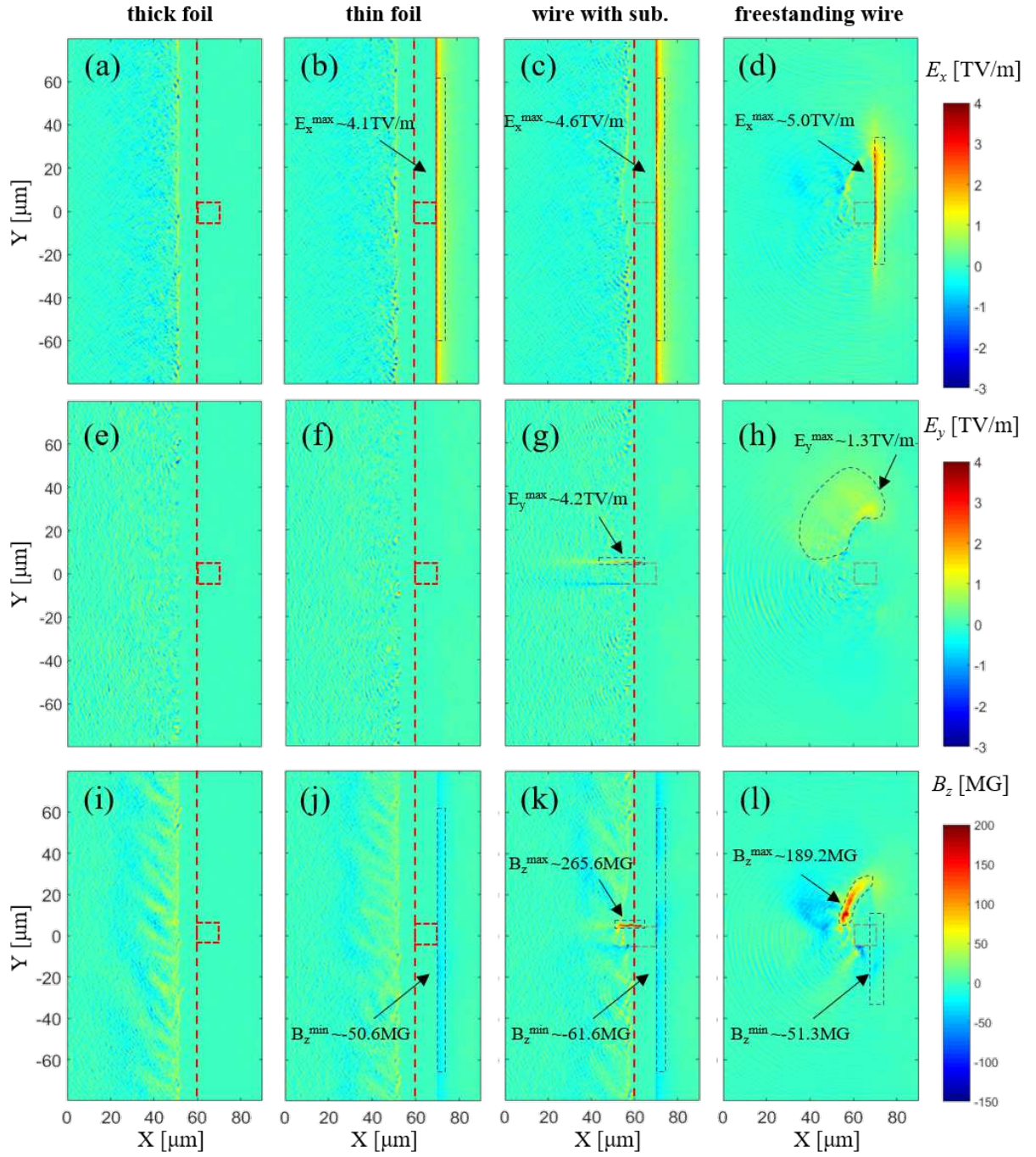
PLEASE CITE THIS ARTICLE AS DOI: 10.1063/1.50023189



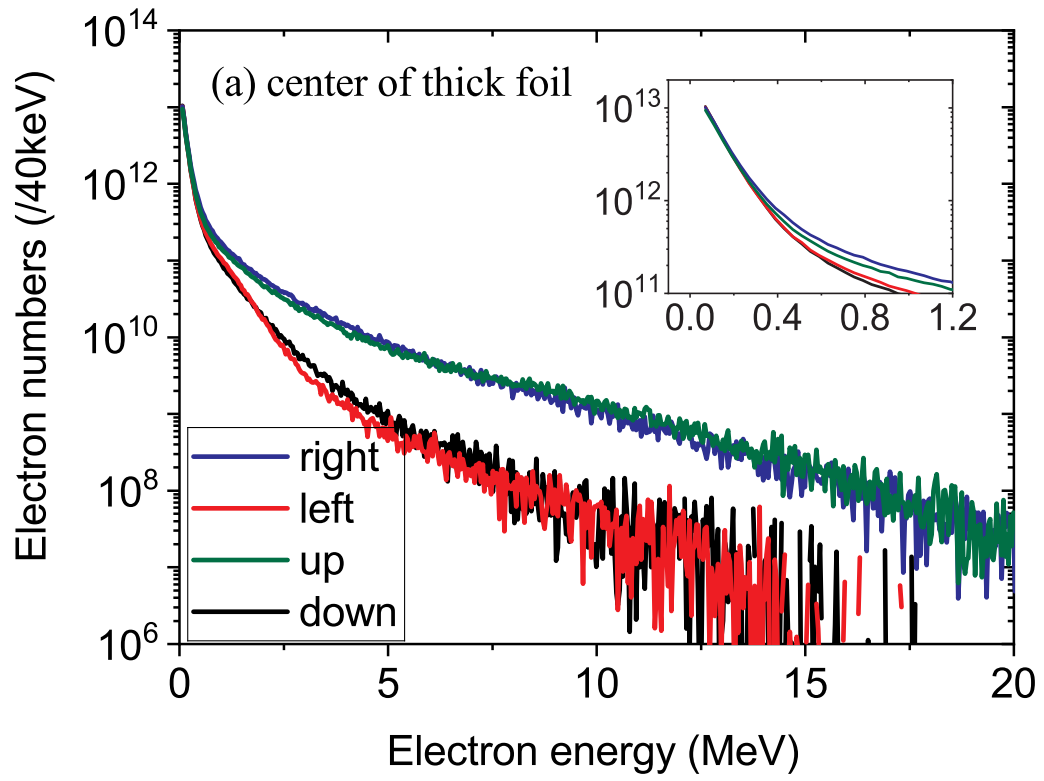


This is the author's peer reviewed, accepted manuscript. However, the online version of record will be different from this version once it has been copyedited and typeset.

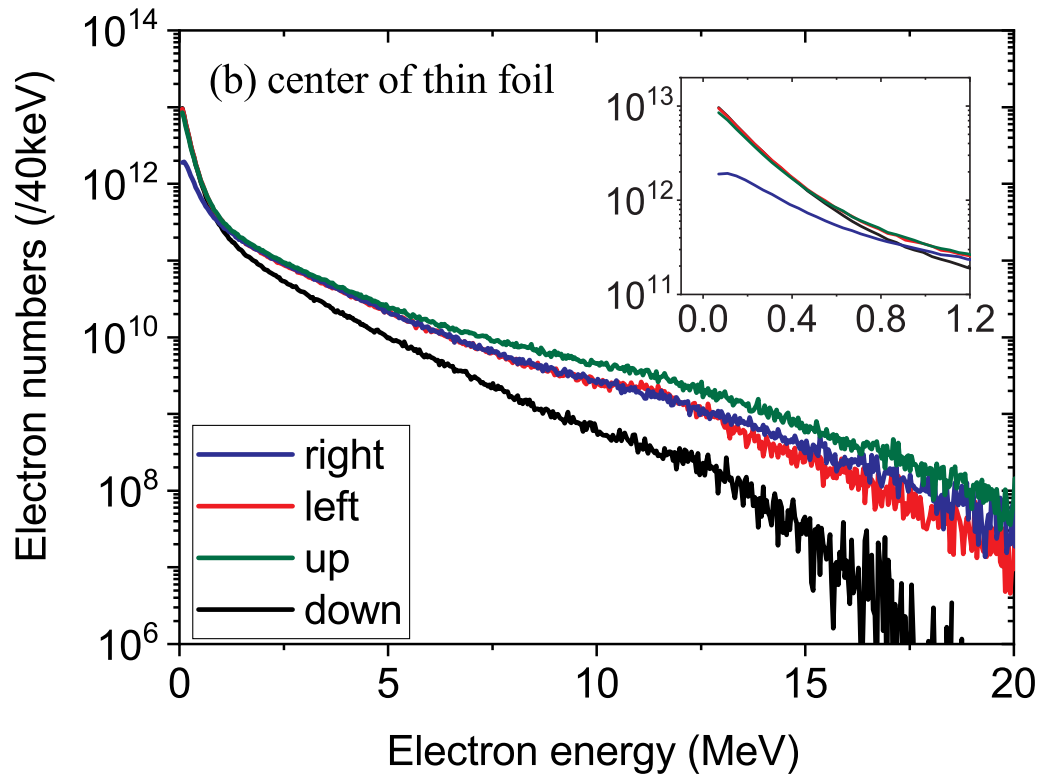
PLEASE CITE THIS ARTICLE AS DOI: 10.1063/5.0023189



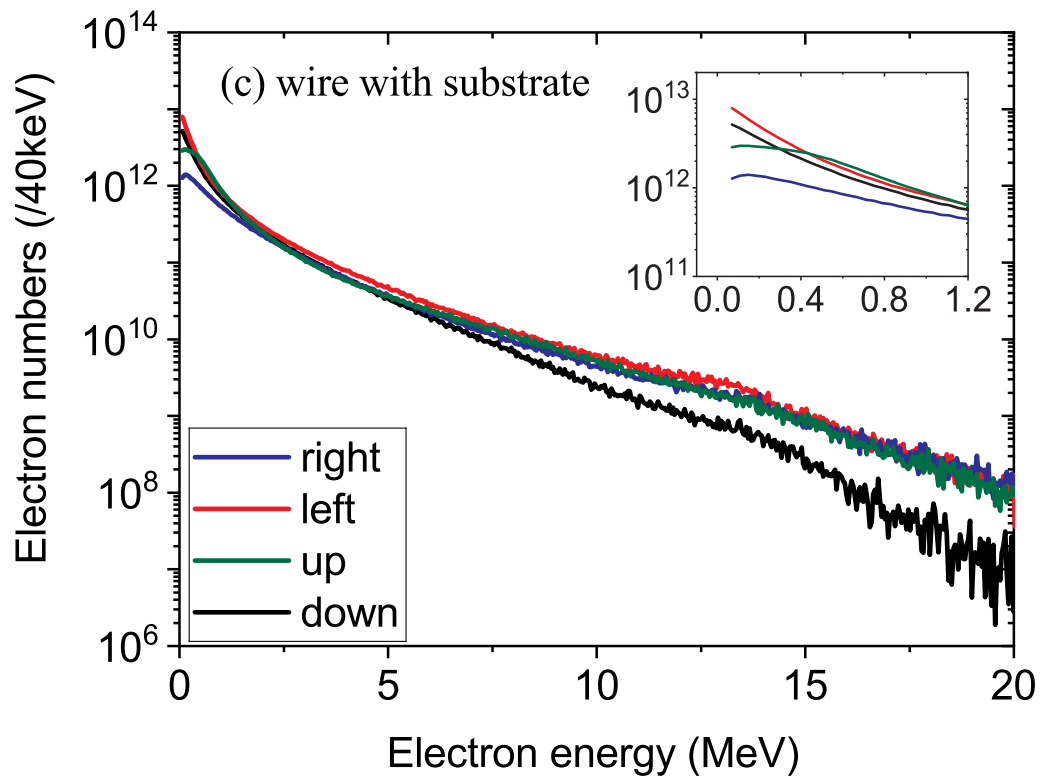
This is the author's peer reviewed, accepted manuscript. However, the online version of record will be different from this version once it has been copyedited and typeset.  
 PLEASE CITE THIS ARTICLE AS DOI: 10.1063/5.0023189



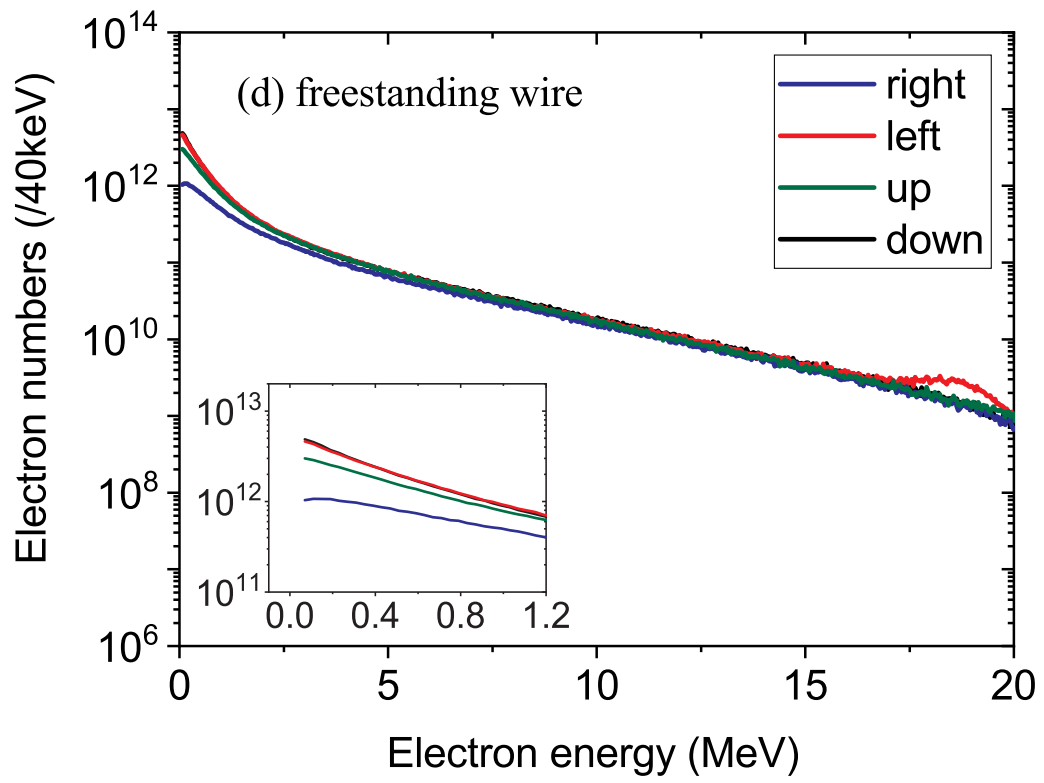
This is the author's peer reviewed, accepted manuscript. However, the online version of record will be different from this version once it has been copyedited and typeset.  
 PLEASE CITE THIS ARTICLE AS DOI: 10.1063/5.0023189



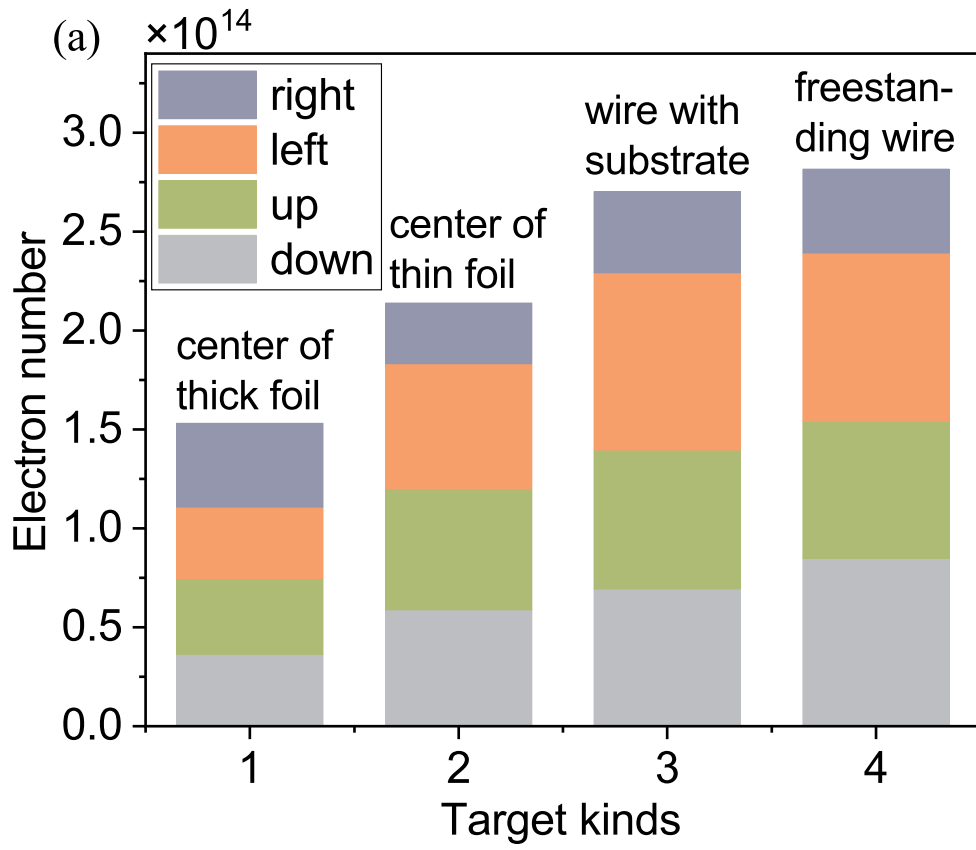
This is the author's peer reviewed, accepted manuscript. However, the online version of record will be different from this version once it has been copyedited and typeset.  
 PLEASE CITE THIS ARTICLE AS DOI: 10.1063/5.0023189



This is the author's peer reviewed, accepted manuscript. However, the online version of record will be different from this version once it has been copyedited and typeset.  
 PLEASE CITE THIS ARTICLE AS DOI: 10.1063/5.0023189

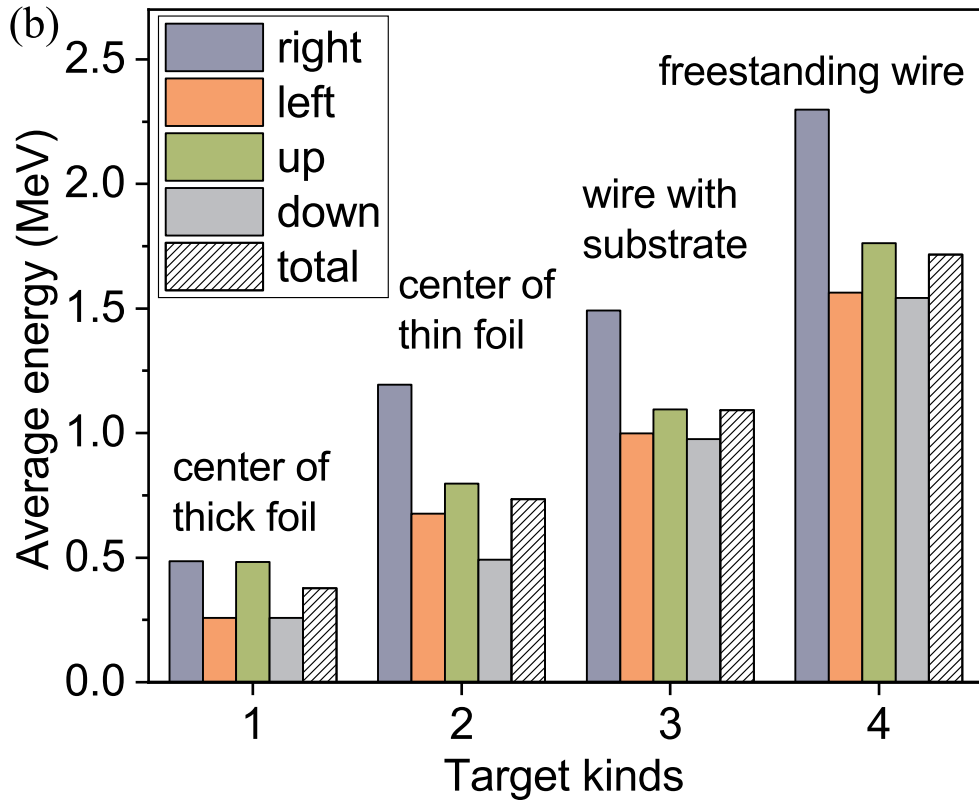


This is the author's peer reviewed, accepted manuscript. However, the online version of record will be different from this version once it has been copyedited and typeset.  
PLEASE CITE THIS ARTICLE AS DOI: 10.1063/5.0023189



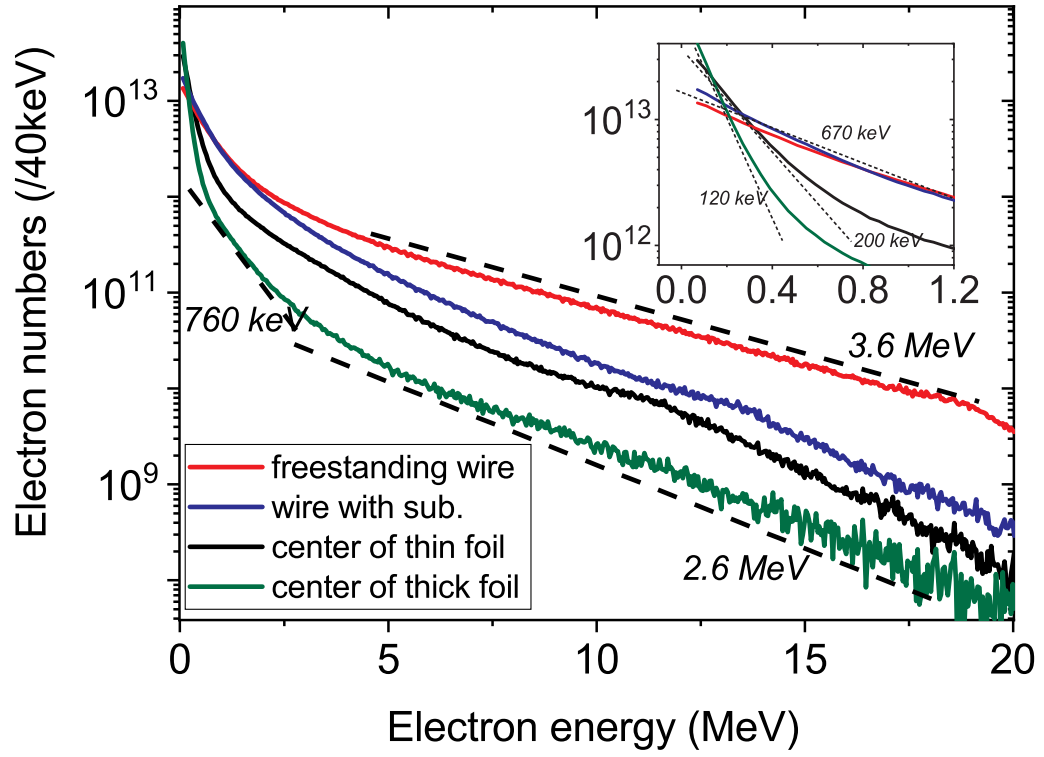
This is the author's peer reviewed, accepted manuscript. However, the online version of record will be different from this version once it has been copyedited and typeset.

PLEASE CITE THIS ARTICLE AS DOI: 10.1063/5.0023189



This is the author's peer reviewed, accepted manuscript. However, the online version of record will be different from this version once it has been copyedited and typeset.

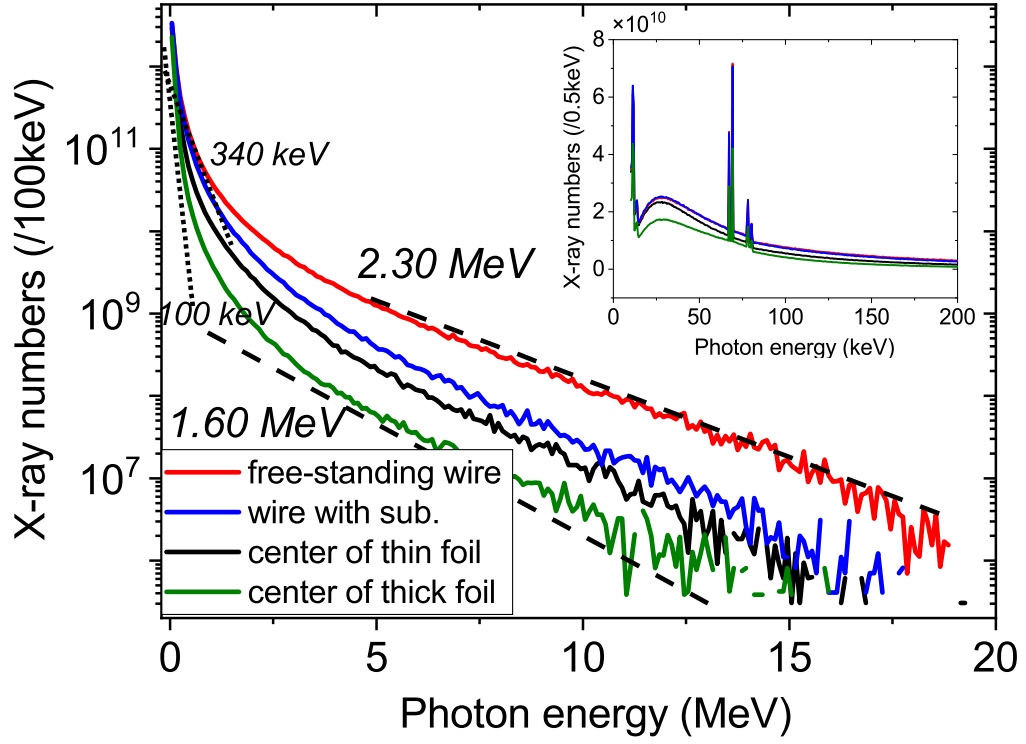
PLEASE CITE THIS ARTICLE AS DOI: 10.1063/1.50023189





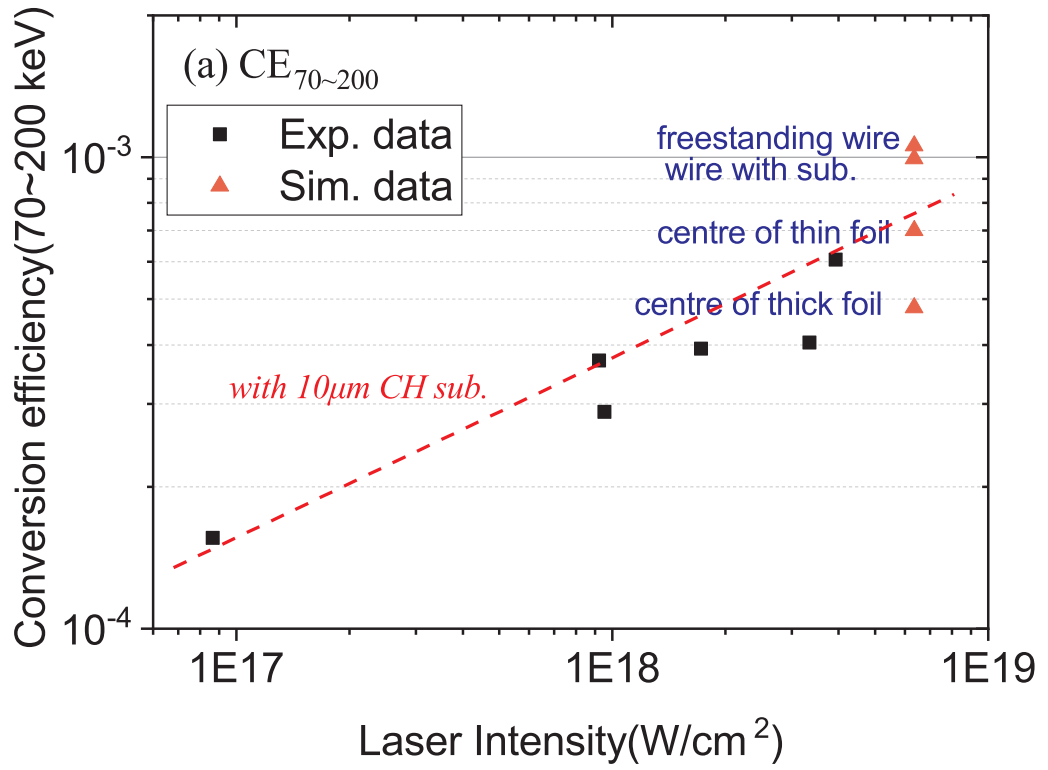
This is the author's peer reviewed, accepted manuscript. However, the online version of record will be different from this version once it has been copyedited and typeset.

PLEASE CITE THIS ARTICLE AS DOI: 10.1063/1.50023189



This is the author's peer reviewed, accepted manuscript. However, the online version of record will be different from this version once it has been copyedited and typeset.

PLEASE CITE THIS ARTICLE AS DOI: 10.1063/5.0023189



This is the author's peer reviewed, accepted manuscript. However, the online version of record will be different from this version once it has been copyedited and typeset.  
PLEASE CITE THIS ARTICLE AS DOI: 10.1063/1.50023189

